

# High Velocity Hail Impact on Composite Laminates – Modelling and Testing

Robin Olsson, Rickard Juntikka, and Leif E. Asp

**Abstract** Hail impact on composite structures during flight occurs at high velocities and is a serious concern as it may cause matrix cracking, large internal delaminations, and eventually fibre fracture not visible on the impacted surface. The present paper gives an introduction to hail impact on composite laminates and an overview of experiments and modelling work on this topic, performed during several years at Swerea SICOMP. Ice balls of different sizes and velocities have been shot with an air gun on composite laminates of different thickness and reinforcement architecture. High speed photography and measurement of strain and deflection histories of the laminates have been used to validate the models developed. Models involve dynamic explicit finite element (FE) simulations with cohesive elements to allow for delamination in the laminate, and simplified but fast analytical models. The experimental response has also been compared with predictions from the FE model and the analytical models using various material models of the ice. FE models using a calibrated elastic–plastic ice model are capable of accurately predicting the response and delamination initiation, while the current analytical models are unable to simulate the initial part of the impact. A main conclusion is that delamination occurs at a very early stage of the impact (first 10–50  $\mu\text{s}$ ) where three-dimensional wave propagation and the initial elastic–plastic behaviour of the ice are important. Closed form models are capable of predicting the peak contact stresses at the first instance of contact, but further work is required to allow simulation of the decay of contact stresses observed in the FE simulations.

**Keywords** Hail impact • Composite • Laminates

---

R. Olsson (✉) • R. Juntikka • L.E. Asp  
Swerea SICOMP AB, Box 104, SE-431 22 Mölndal, Sweden  
e-mail: [robin.olsson@swerea.se](mailto:robin.olsson@swerea.se)

R. Juntikka  
FS Dynamics Sweden AB, Mölndalsv. 24, SE-412 63 Gothenburg Sweden

## 1 Introduction

### 1.1 Significance of Hail Impact

Hail and bird impact on engines and leading edges of wings and tail of aircraft in flight is a serious concern for designers due to the relatively high impact velocities. Impact by large birds is normally the most severe case, but will usually immediately be noticed and addressed. In contrast hail impact is relatively common, involves multiple impact sites and the resulting damage will in many cases remain undetected. A thorough, but fairly old review of the topic was given in [1]. Some examples of subsequent work may be found in [2]. The threat of hail impact on aircraft was recently addressed in a report to the European Aviation Safety Agency (EASA) [3]. Leading edges of aircraft are thus exposed to high velocity impact, but tend to be well protected and are rarely a part of the primary structure. Falling hail may cause severe damage to aircraft parked on ground, as the terminal impact velocity of large hail still is significant, Fig. 1, and the upper surfaces of fuselage and wings are less well protected against impact.

### 1.2 Effects of Hail Impact on Composite Structures

Impact damage is a particular concern for fibre reinforced composite laminates, which are sensitive to out-of-plane loading (e.g. impact) and may suffer extensive internal damage without any visible surface damage. The visibility is further reduced by impact of comparatively soft bodies like birds and ice, which produce less visible dents. Impact damage in composites typically involves cracks along

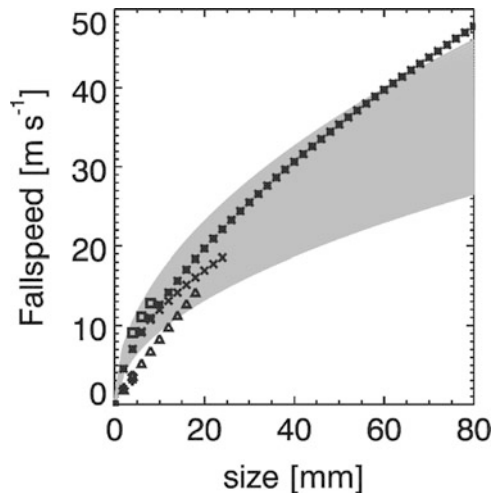


**Fig. 1** Empirical (*symbols*) and theoretical (*grey range*) for  $0.5 < C_d < 1.5$  fall speeds for graupel and hail [3] © EASA. Reprinted with permission

the fibres (matrix cracks) and separation of plies (delamination), but may also involve fibre fracture, and may reduce the strength to 1/3 of the undamaged strength, particularly in compression [4].

The increasing use of composite materials in aircraft primary structures has caused a growing concern for the effect of hail impact on such structures. For this reason the aviation safety authorities FAA and EASA have initiated studies to define the threat of hail impact and its effect on structures, e.g. [3], with the aim to develop improved guidelines. Most work on hail impact has been focused on thin sheet metallic structures, while only a few studies have considered laminated composite structures.

Mahinfalah and Skordahl [5] compared the fatigue life of 2 mm quasi-isotropic carbon/epoxy laminates impacted by 25.4–38.2 mm diameter hail at the terminal velocity in free fall ( $\sim 45$  m/s) and by 12.7 mm aluminium balls having the same kinetic energy. The ice balls caused no delaminations and no reductions in fatigue life of the laminates, while the aluminium balls caused noticeable reductions in the fatigue life. The damage inflicted by the aluminium balls was incorrectly contributed to their rigidity, but the main cause appears to have been that they were fired at a significantly higher velocity (71–139 m/s). It has been shown that delamination onset during small hard mass impact occurs at a specific threshold load [6] and that this load is virtually linearly proportional to the impact velocity, while the influence of impactor mass is negligible [7]. Hence, *the impact energy is not a relevant measure of impact severity*.

Kim and co-workers have performed extensive experimental studies and simulations of impact by artificial hail, focused on the impact response and resulting damage. The studies include quasi-isotropic layups of AS4/977 and AS4/8552 carbon/epoxy woven prepreg [8], quasi-isotropic layups of T800/3900-2 carbon/epoxy UD tape prepreg [9] and single lap joints with cross-ply carbon/epoxy UD tape prepreg [10]. Very similar delamination threshold velocities were obtained for the woven systems and for the UD-tape system.

Appleby-Thomas et al. [11] studied carbon/epoxy quasi-isotropic layups of a G0926/5 woven fibre system with an RTM-6 matrix, and a stitched triaxial NCF system with a 790 RTM matrix, manufactured using the RTM process. The plates were impacted using cylindrical ice impactors with a hemispherical front end and impacted plates were inspected using ultrasonic C-scan. The residual strength was evaluated in Compression After Impact (CAI) tests using a modified ASTM procedure, where the load only was applied over a portion of the specimen edge. Single and repeated impacts were performed to simulate the possibility of multiple hail impacts. It was found that repeated impacts resulted in a growing delamination area, essentially proportional to the cumulated energy. It is, however, hard to judge if the growth was a result of several impacts at a single point or due to several nearby impacts. Low velocity (drop-weight) impact tests [12] demonstrated that repeated impacts in a single location not causes further damage growth, while several neighbouring impacts result a superposition of delaminations for the corresponding single impacts. Appleby-Thomas et al. [11] found that the impact energy required to initiate delamination was higher for the woven architecture, and that the delamination areas and strength reductions typically were smaller for a given

energy level. A higher interlaminar toughness and less delamination is familiar from other studies of woven materials, but the two fibre architectures studied by Appleby-Thomas et al. are not directly comparable, due to differences in resin systems.

The current paper gives an overview of studies on hail impact on composites performed during 2005–2011 at Swerea SICOMP, mainly within various collaboration projects with Volvo Aero Corporation. The overview covers both previously presented work [13–15] and some previously unpublished work. This chapter is organised as follows; first an overview is given of the formation, properties and modelling of hail, secondly our experimental studies of hail impact on composite laminates are presented. This is followed by comparisons with the finite element (FE) simulations and analytical models developed at Swerea SICOMP. Finally, causes for disagreement between analytical models, FE models and experiments are discussed and areas for improvements are indicated.

## **2 Formation, Properties and Modelling of Hail**

### ***2.1 Hail Formation***

By convention hail is defined as balls or irregular lumps of ice with a diameter of 5 mm or more [16]. Smaller pieces of ice of the same origin are called ice pellets. Smaller pieces of softer particles, typically 2–5 mm, are called snow pellets (graupel). The formation of hail is dependent on a rather specific type of weather system with strong updraft winds [17]. Strong updraft winds are present in a type of cloud called cumulonimbus (“thunderclouds”), which mostly appear in the summer. Clouds in general are created through condensation, which is related to the amount of water that air can sustain which in turn depends on temperature. The sun-warmed surface of the earth heats the surrounding damp air, which then expands and rises into the atmosphere. As it expands and cools it becomes saturated with water and eventually starts to precipitate creating tiny nuclei. Water droplets are then formed through condensation on these nuclei and small particles such as microorganisms, dust or pollen, thus making up the base of a cumulus cloud. Through combination of several cumuli a very strong, warm and humid updraft can be created with wind velocities of more than 160 km/h. This convection process creates thunderclouds which can expand over an altitude ranging from 2 to more than 15 km.

Within the thunderclouds the temperature will vary depending on the altitude, ranging from +10 to –60°C. At lower altitudes the cloud consists of droplets while at high altitudes the droplets form ice crystals. Within the given altitude interval an important phenomenon in cloud physics called super cooling occurs. Super cooling is a condition where drops of water can remain liquid at temperatures as low as –40°C. The presence of small particles in the super-cooling zone is the origin of hail formation through the fusion of droplets and the particles. The surrounding droplets, raindrops or soft hail build on the formed hail nuclei and the hail will gain altitude as the updraft increases and fall due to gravity. The dynamics of the storm

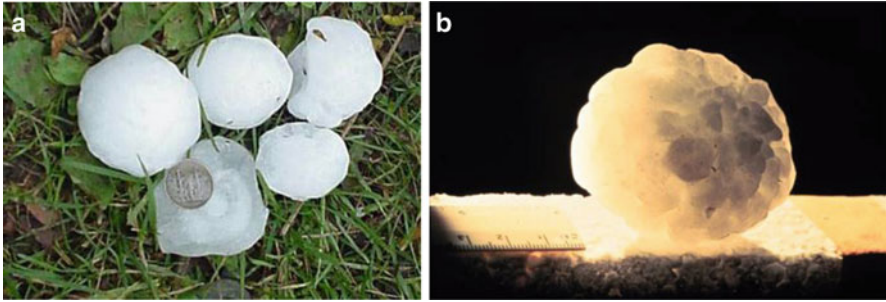


**Fig. 2** Different types of hailstones; (a) Onion-layered [18]; (b) Fusion of several soft hail particles [19]

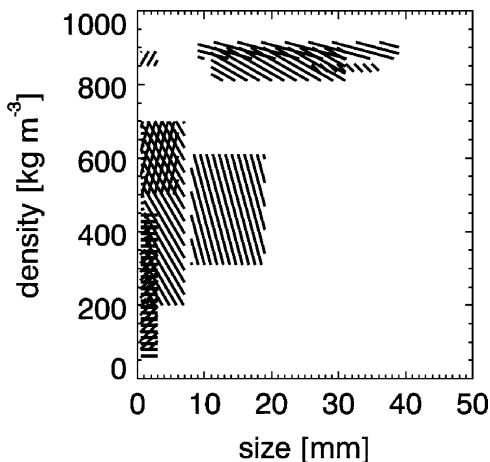
and the level of the updraft determine the continuation or the end of hail formation. If the updraft is below a certain level the hail will fall to the ground as rain or soft hail. However, if the updraft is sufficiently strong the hail particles continue to grow as they move up the continuously colder layers. Finally, when the updrafts can no longer support the weight of the hailstones or if they catch a downdraft they fall heavily to the ground, reaching speeds of up to 100 km/h for a 40 mm hailstone.

As mentioned, the hail grows either by fusion of hail nuclei and droplets, raindrops or soft hail. Depending on the growth process different hail types are formed. If the hail growth is mainly conducted within the region where super cooling is present the resulting hailstone becomes oblate spherical and “onion-layered”, see Fig. 2a. This is particularly evident in larger hailstones. These layers usually alternate between opaque ice and clear ice. An opaque ice layer forms when the hailstone collects small, super cooled liquid droplets that freeze rapidly on impact, thereby trapping air bubbles within the ice and giving it a “milky” texture. This is called dry growth. When larger super cooled water drops impact on a hailstone, the freezing is slower, allowing the air bubbles to escape, and thus forming clear ice. This is called wet growth. The other type of hailstone is formed through fusion of snow pellets, thus forming a hailstone of irregular structure consisting of a number of small snow pellets (graupel), see Fig. 2b.

## 2.2 *Mechanical Properties of Hail*

It is rather difficult to find scientific investigations regarding mechanical properties of hail in the literature. There are some data on weight and dimensions of collected hailstones [3], but there appears to be a lack of direct tests of the mechanical properties of hail. As mentioned previously, the formation of hailstones can vary significantly, certainly giving varying mechanical properties of the hailstone. The structure of a hailstone depends on a number of variables present in the forming process such as droplet sizes, temperature, time of flight and level of updraft. It has been observed that hailstones may have an onion like structure, with layers of

**Fig. 3** Experimentally determined densities for graupel and hail [3] (© EASA. Reprinted with permission)



different density. The measured density of hail is in the interval of 300–900 kg/m<sup>3</sup>, Fig. 3 [3]. The lower density is close to the maximum density of snow and the upper boundary is close to the density of clear ice. Due to the limited understanding of the properties of hail it is hereafter assumed that the worst-case hail impact scenario is represented by hailstones consisting of polycrystalline freshwater ice (clear ice).

The properties of ice has been an area of extensive research due to the need for relevant data in a wide variety of research areas, such as climatology, glaciology, avalanche research, comet research and studies of man-made structures in cold regions. Ice appears with a wide range of crystal structures, e.g. columnar-grained freshwater or saline (sea) ice, and random-grained polycrystalline freshwater ice (clear ice), which result in different degrees of anisotropy [20]. For extensive reviews, see e.g. [21] or [22].

In general ice is viscoelastic rather than elastic and the properties of ice strongly depend on temperature and loading rate [23–25]. Furthermore, the strength of ice is highly dependent on the hydrostatic stress component and the triaxial stress state [26]. Finally, there is a strong size effect, where the strength increases with decreasing size of the stressed volume, both in tension [23] and in compression [27]. Thus, a full characterisation of ice requires consideration of the type of ice, the temperature, loading rate and size effects for a wide range of stress states.

Polycrystalline freshwater ice (*clear ice*) is obtained by freezing water under ambient temperature and pressure, and has a hexagonal crystal structure with a density of around 900 kg/m<sup>3</sup>. The structure results in a moderate anisotropy with a Young's modulus ranging from approximately 6 to 12 GPa along its most and least compliant direction respectively, and with a Poisson's ratio of around 0.33. Several studies have examined the properties of ice during uniaxial loading of ice cylinders with various aspect ratios. Experiments show a ductile behaviour in tension at low strain-rates and a brittle behaviour at intermediate and high strain-rates, Fig. 4 [21, 26]. Compressive stress–strain curves have shown ductile behaviour at low and

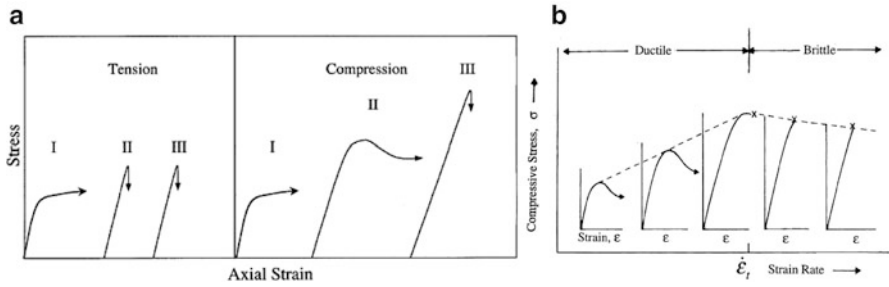


**Fig. 4** Influence of strain-rate on the tensile and compressive stress–strain behaviour of ice. *I, II* and *III* denote low, intermediate and high strain-rate respectively. (a) [21] © Kluwer Academic Publisher. Reprinted with permission. (b) [26] © Elsevier. Reprinted with permission

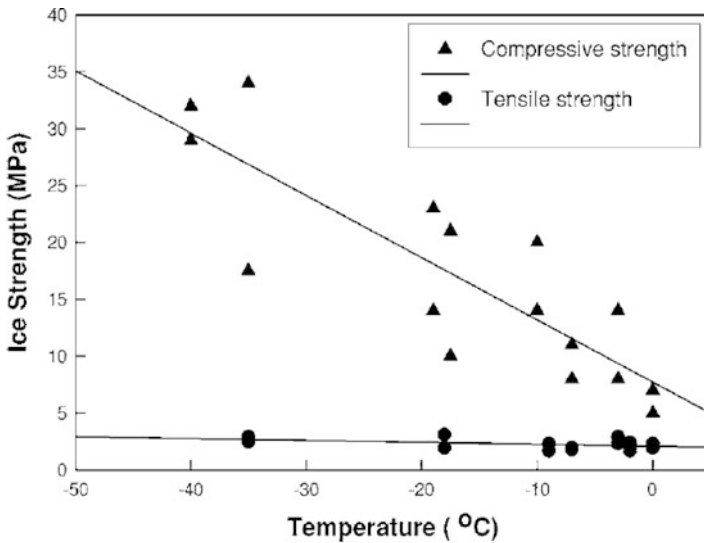


**Fig. 5** Influence of temperature on compressive and tensile strength of ice [23] © Kluwer Academic Publisher. Reprinted with permission

intermediate strain-rates, but brittle behaviour at high strain-rates, Fig. 4. The compressive strength exhibits a relatively strong dependence of temperature, Fig. 5 [23] and strain-rate, Fig. 6, [24] whereas the tensile strength is much lower (about 1 MPa) and relatively insensitive to changes in temperature strain rate and temperature [23]. In general the compressive strength increases as the temperature decreases and/or the strain-rate increases. Some earlier studies indicated a decreasing compressive strength after a peak at a strain-rate of approximately  $10^{-3}$ /s, which coincides with a transition from ductile to brittle behaviour, Fig. 4. These results are contradicted by later results in [24] obtained in the range 400–2600/s using a split Hopkinson

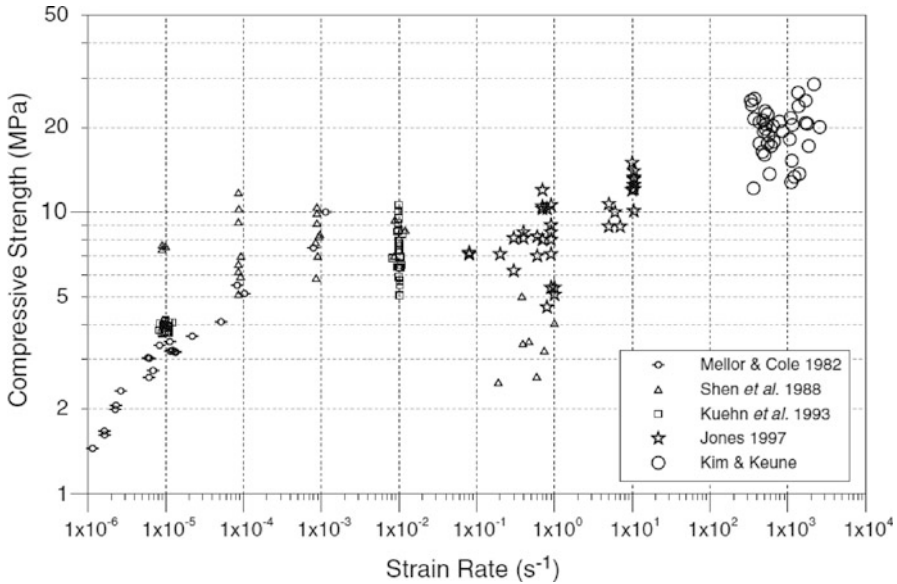


**Fig. 6** Influence of strain-rate on the compressive strength of ice [24] © Kluwer Academic Publisher. Reprinted with permission

bar test, and by tests in [28] at strain rates of  $10^{-3}$ – $10^{-1}$ /s, where the compressive strength was fitted to a power-law of the form  $\sigma = A\dot{\epsilon}^m$ , with  $A = 8.9$  and  $m = 0.15$ .

The qualitative trends in Figs 5 and 6 have been confirmed by other studies, e.g. [29], but there is a large scatter in material data due to lack of standardised test specimens and evaluation methods. Thus a compressive strength of atmospheric ice as low as 1 MPa at  $-2^\circ\text{C}$  and a strain rate  $4.3 \cdot 10^{-2}$ /s was found in [30].

Sea ice is anisotropic (results from vertical growth direction), contains salt and has a larger porosity. The strength appears to be somewhat lower than the polycrystalline freshwater ice in hail, although the qualitative influence of temperature and strain rate is similar. Thus, [31] found a tensile strength of 0.61 MPa at  $-5^\circ\text{C}$  and 0.75 MPa at  $-20^\circ\text{C}$ , both tested at  $10^{-3}$ /s. The compressive strength increased from 4.67 MPa at  $-5^\circ\text{C}$  to 8.24 MPa at  $-20^\circ\text{C}$ , both tested at  $10^{-3}$ /s.

The increasing strength at lower temperatures appears to be a combined effect of an increasing stiffness and increasing failure strains. Table 1 provides a comparison of reported Young's moduli and failure strains of two different types of ice. It should be noted that the properties of freshwater ice were calculated using the crosshead displacement, which indicates that the true modulus and failure strain might be substantially closer to the values reported for sea water.

As mentioned earlier, the strength of ice is strongly dependent of the strain rate and applied stress state, which is also indicated by the large differences in tensile and compressive strength. Impact of spherical ice balls will result in a triaxial stress

**Table 1** Reported Young’s modulus and failure strain of freshwater ice and sea ice

Property	Freshwater ice <sup>a</sup>		Sea ice <sup>b</sup>	
Density, $\rho$ [kg/m <sup>3</sup> ]	~900		865	
Tensile Young’s modulus [GPa]			6.6	-5°C; 10 <sup>-3</sup> /s
			7.3	-20°C; 10 <sup>-3</sup> /s
Compressive Young’s modulus [GPa]	1.6 <sup>c</sup>	-10°C; 4.10 <sup>-4</sup> /s	6.2	-5°C; 1.10 <sup>-2</sup> /s
	2.8 <sup>c</sup>	-33°C; 4.10 <sup>-4</sup> /s	7.5	-20°C; 1.10 <sup>-2</sup> /s
Compressive failure strain [%]	0.50 <sup>c</sup>	-10°C; 4.10 <sup>-4</sup> /s	0.07	-5°C; 1.10 <sup>-2</sup> /s
	0.64 <sup>c</sup>	-33°C; 4.10 <sup>-4</sup> /s	0.12	-20°C; 1.10 <sup>-2</sup> /s

<sup>a</sup>[29]

<sup>b</sup>[31]

<sup>c</sup>Based on cross-head displacement

**Table 2** Material properties assumed in evaluation of the analytical model

Ply properties of assumed carbon/epoxy material		Quasi-brittle ice [32]	
Density, $\rho_c$ [kg/m <sup>3</sup> ]	1,520	Density, $\rho_i$ [kg/m <sup>3</sup> ]	846
Longitudinal Young’s modulus, $E_{11}$ [GPa]	133	Young’s modulus, $E_i$ [GPa]	9.19
Transverse Young’s moduli, $E_{22} = E_{33}$ [GPa]	10.0	Poisson’s ratio, $\nu_i$	0.33
Poisson’s ratio, $\nu_{12} = \nu_{13}$	0.27	Yield strength, $\sigma_Y$ [MPa]	10.3
Transverse Poisson’s ratio, $\nu_{23}$	0.44	Hardening modulus, $E_{pl}$ [GPa]	6.89
In-plane shear moduli $G_{12} = G_{13}$ [GPa]	4.8	Bulk modulus, $K_i$ [GPa]	8.99
Transverse shear modulus, $G_{23}$ [GPa]	3.5	Plastic failure strain, $\epsilon_{plF}$ [%]	0.35
Transverse tensile strength, $T$ [MPa]	50	Ultimate stress, $\sigma_F$ [MPa]	34.4
Shear strength, $S$ [MPa]	75	Tensile failure pressure, $p_i$	-4.0
Interlaminar tensile toughness, $G_{Ic}$ [J/m <sup>2</sup> ]	421		
Interlaminar shear toughness, $G_{IIc} = G_{IIIc}$ [J/m <sup>2</sup> ]	1,420		

state, where the constitutive behaviour may differ significantly from the behaviour in uniaxial compression.

A practical approach to determine the constitutive parameters for the triaxial stress state during impact is to shoot ice balls on instrumented plates or flat load cells, and to use dynamic FE simulations to fit an appropriate constitutive model to the experimental results. This approach was used in [32] where hail impact experiments were performed on composite plates using manufactured ice balls with a temperature of -17°C. The experiments were simulated using the explicit software programme LS-Dyna 3-D employing material type 13, elastic-plastic with failure. Basic material inputs were collected from the literature but certain values for input, such as hardening modulus etc., were parametrically determined by comparing the numerical simulations with the experimental data. The simulation results were consequently in very good agreement with experiments. The resulting material properties have been listed in the right part of Table 2. The current authors successfully applied a similar approach during modelling of in-house experiments [14]. Key parameters of the material model were determined through a factorial parameter study and were fitted to a few benchmark tests, but the model details are commercially confidential.

According to [32] measurements of the adiabatic shock Hugoniot curves (pressure–volume relationship) of ice in [33] showed that an extremely large pressure (23.5 GPa) is required to cause a phase change from solid to liquid states. In the context of ice projectiles, there is insufficient confinement to allow such large pressure build-up. Therefore impacting ice is not expected to undergo phase change.

### ***2.3 Manufacture of Artificial Hail***

Various approaches have been used to manufacture ice samples. Kim and Kedward [32] produced monolithic and layered ice balls by using spherically shaped two-part moulds. The layered ice is slightly tougher than monolithic ice and was manufactured to simulate hail with a spherically layered “onion-like” structure. Due to manufacturing difficulties the layered ice balls were produced with flat layers of equal thickness through the diameter. When firing the ice spheres towards panels the impacting direction was aligned normal to the flat layers. Kim et al. [8] simply used a spherical split mould having a filling hole and after filling them up with water, the spheres were kept frozen at a temperature of  $-26^{\circ}\text{C}$ . Arakawa and Maeno [29] compacted fine ice particles in a vessel at 7 MPa and  $0^{\circ}\text{C}$  at a pressure of 100 Pa below that of the atmosphere, which resulted in samples that were almost bubble free. A more than sophisticated way of the manufacturing procedure is the method used in [30]. They used a wind tunnel where they installed an aluminium collector, which they sprayed with water droplets using a water nozzle. The aim of the work was to investigate the influence of different atmospheric conditions on the mechanical properties of atmospheric ice. Weiss and Schulson [34] used presieved seeds and distilled, deionised and degassed water. An aluminium rectangular mould was filled with fragments of one size of ice in order to control the grain size, and was then evacuated at  $0^{\circ}\text{C}$  over 3 h. Afterwards, the water was passed slowly through the mould and the ice-water mixture was frozen radially inward using cooling plates at  $-5^{\circ}\text{C}$  attached to the sides of the mould. The resulting porosity was low ( $<0.2\%$ ). To receive a reasonably low porosity in freezing ice resembling clear ice it seems to be sufficient to use a mould and freeze the samples in under-pressure conditions.

### ***2.4 Influence of Impactor Shape***

The type of ice and shape of impactors typically used in hail impact tests can affect the representativeness of these tests compared to a “real-life” impact. Combescure et al. [35] performed a series of high and low velocity impact tests on a rigid support and flexible aluminium plates using flat or conical impactors made of monocrystalline and polycrystalline ice. In cases of conical (or inclined flat) ice

impactors, the failure mode was always by cleavage while fine fragmentation was found for flat impactors. For a given impact velocity, the permanent deformation of the aluminium plates was greater in cases involving fragmentation, i.e. for flat impactors, which appear to represent a “worst-case” scenario as far as the impactor shape is concerned. Increasing velocity resulted in increased permanent deformation of the aluminium plates and smaller ice fragments.

A characteristic of ice impact is that the fragmentation of the impactor results in a large area of the impacted component being affected by the dynamic loading. The deflection of ice fragments instantly after impact was investigated in [36]. Impact tests of spherical ice impactors of several diameters were performed on rectangular plates, which could be tilted to offer different incident angles. The authors report that at the moment of impact, fragments from the front of the ball form a low density chaotic cloud which then evolves into a higher density, disk shaped cloud. The deflection angle was insensitive to the incident impact angle or impactor diameter and was relatively shallow ( $\sim 1^\circ\text{--}2^\circ$ ) with respect to the impacted surface. It was found that the cloud travels at a velocity close to the tangential impact velocity while preserving a disk shape.

## 2.5 *Material Models for Hail*

Various material models have been developed for numerical modelling of hail. The elastic–plastic model with brittle failure in [32] has already been mentioned. A modified version of this model was used by the current authors [14]. A more advanced ice model was developed in [37], as a part of the NASA investigations after the disaster with the space shuttle “Columbia”. The model accounted for independent failure stresses in tension and compression, strain rate sensitivity of the flow stress, the ability of the failed ice to continue to carry hydrostatic stress and use of an Eulerian mesh, but did not consider effect of temperature. It was noted that consideration of the lower failure stress in tension would be of particular importance for non-spherical impactors, where the failure is no longer entirely controlled by compressive stresses. The model was based on interpolation of tabulated experimental data rather than on analytical relations for an assumed material model. A good agreement was shown for a range of different impacts on fixed load cells. Comparisons with alternative ice models were limited but it was noted that the model was able to successfully predict the fragmentation during impact by ice cylinders, in contrast to an elastic–plastic model of the type used in [32] and [14], which had been tuned for pressure dominated stress states during impact by ice spheres.

Chuzel et al. [38] developed a material model for ice and compared it to data from tests at low strain rates ( $\leq 50/\text{s}$ ) in [35]. The model is based on an isotropic damage model for concrete which assumes a linear elastic behaviour before failure initiation and uses an exponential softening law to handle progressive damage. The damage model features independent damage variables in tension and compression

and a regularization scheme for mesh objectivity. The model was implemented in LS-DYNA and used with an SPH formulation. It correlated well with results in [35], even though the SPH grid appears rather coarse to accurately capture the different wave features appearing during impact.

A material model for ice was also developed in [39], but the model was not applied to impact simulations. The model uses a continuum damage approach to model the brittle behaviour of ice and includes a plastic response with strain rate dependency. The model was implemented in an explicit FE code and used with standard solid elements. Failure locus for biaxial loading was predicted and in good agreement with experimental data. The model was also verified on three point bend tests but no correlation with experimental data was presented.

The developments in [38] and [39] indicate that accounting for the brittle cracking through progressive damage is important for the modelling of the ice material. Both models are based on models used for concrete, and even though the model in [39] includes features specific to the ice material (e.g. plasticity and strain rate), the physical basis of the models is rather unclear. To handle mesh objectivity a regularization scheme was used in [39]. However, both the regularization value and the characteristic length needs to be adjusted for a given mesh configuration, which can cause problem for irregular meshes and also raise the question of the actual fracture energy being spent to progress damage.

## 3 Experiments

### 3.1 *Aims and Content*

The experimental studies of ice impact have been conducted in close collaboration with Volvo Aero Corporation in Sweden. Most of these studies have been linked to investigations of candidate composite materials for outlet guide vanes (OGV) in the FP6 VITAL project [40]. One of the aims of this project was to demonstrate the possibility to use polymer composites in structural components of jet engines for future passenger aircraft. Based on the impact threat expressed by the aero engine manufacturers in the VITAL project the OGV must sustain normal impacts from 50 mm diameter ice at velocities exceeding 100 m/s (normal to the OGV). The experimental investigations aimed to compare and judge the merits of different composite materials and fibre architectures for their impact resistance to realistic threats from hail and runway debris.

### 3.2 *Specimens*

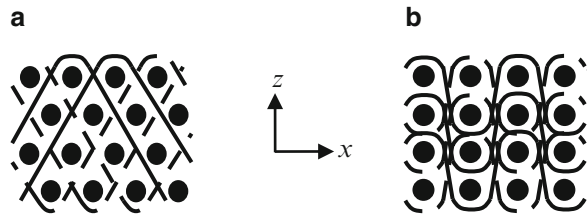
Several different composite materials were impacted using ice spheres and/or stones:

**Table 3** Material properties of carbon/vinylester NCF assumed for predictions in Fig. 22

Ply properties of carbon/vinyl ester NCF	
Density, $\rho_c$ [kg/m <sup>3</sup> ]	1,520
Young's moduli, 0° or 90° plies, $E_{11}$ [GPa]	100 <sup>a</sup>
Young's moduli, $\pm 45^\circ$ plies, $E_{11}$ [GPa]	116 <sup>a</sup>
Out-of-plane Young's modulus, $E_{22} = E_{33}$ [GPa]	7.6 <sup>a</sup>
Poisson's ratio, $\nu_{23}$	0.31 <sup>a</sup>
In-plane Poisson's ratio, $\nu_{12} = \nu_{13}$	0.36 <sup>a</sup>
In-plane shear moduli $G_{12} = G_{13}$ [GPa]	2.9 <sup>a</sup>
Transverse shear modulus, $G_{23}$ [GPa]	2.9 <sup>a</sup>
Transverse tensile strength, $T$ [MPa]	50 <sup>b</sup>
Shear strength, $S$ [MPa]	75 <sup>b</sup>
Interlaminar tensile toughness, $G_{Ic}$ [J/m <sup>2</sup> ]	577 <sup>c</sup>
Interlaminar shear toughness, $G_{IIc} = G_{IIIc}$ [J/m <sup>2</sup> ]	1,152 <sup>c</sup>

<sup>a</sup>[41]  
<sup>b</sup>Assumed  
<sup>c</sup>[42]

**Fig. 7** Architecture of tested 3D weaves: (a) Angle interlock (AI), (b) Layer-to-layer interlock (LTL)



1. Quasi-isotropic  $[0^\circ/90^\circ/45^\circ/-45^\circ]_{s3}$  non-crimp fabric (NCF) carbon fibre/vinyl ester (Norpol DION 9500–501) laminates of thickness 5.4 mm. The preform was a biaxial carbon fibre NCF (Devold AMT LT450 and DB450, 205 g/m<sup>2</sup> in each direction).
2. Quasi-isotropic non-crimp fabric (NCF) carbon fibre/epoxy laminates with nominal thickness 4 and 6 mm.
3. Orthotropic plain weave (PW) AS7-J/RTM6 carbon fibre/epoxy laminates with nominal thickness 4 mm.
4. Orthotropic 3D weave, angle interlock (AI) AS7-J/RTM6 carbon fibre/epoxy with nominal thickness 5 mm.
5. Orthotropic 3D weave, layer-to-layer interlock (LTL) AS7-J/RTM6 carbon fibre/epoxy with nominal thickness 4 mm.

The properties of material 1 are listed in Table 3. The weave reinforced composites were orthotropic and contained only fibres in the 0°/90° directions. The two 3D weaves (angle and layer-to-layer interlocks) are schematically depicted in Fig. 7, and were selected to achieve two laminates with considerably different shear stiffness.

All laminates were made by vacuum infusion of a resin into dry fibre preforms and had a fibre volume fraction between 50 and 55%. Measured and predicted homogenised in-plane and out-of-plane tensile properties for the different materials are listed in Table 4.

**Table 4** Predicted homogenised in-plane properties for the various laminates

Property	CF/Vinyl ester	CF/epoxy	AI	LTL
	NCF	NCF	3D weave	3D weave
Density, $\rho$ [kg/m <sup>3</sup> ]	1,530 <sup>a</sup>	1,520 <sup>a</sup>	1,510 <sup>c</sup>	1,495 <sup>c</sup>
Fibre volume fraction, $v_f$	55 <sup>a</sup>	55 <sup>a</sup>	50 <sup>c</sup>	55 <sup>c</sup>
Young's modulus, $x$ -direction, $E_x$ [GPa]	$\approx 39^a$	$\approx 52^a$	79 <sup>b</sup> /25 <sup>c</sup>	97 <sup>b</sup> /96 <sup>c</sup>
Young's modulus, $y$ -direction, $E_y$ [GPa]	$\approx 39^a$	$\approx 52^a$	51 <sup>b</sup>	51 <sup>b</sup>
Young's modulus, $z$ -direction, $E_z$ [GPa]	$\approx 7.6^a$	$\approx 10^a$	16 <sup>b</sup>	12 <sup>b</sup>
Shear modulus, $G_{xy}$ [GPa]	$\approx 16^a$	$\approx 20^a$	6.2 <sup>b</sup>	6.1 <sup>b</sup>
Shear modulus, $G_{yz}$ [GPa]	2.9 <sup>a</sup>	4.1 <sup>a</sup>	5.2 <sup>b</sup>	4.9 <sup>b</sup>
Shear modulus, $G_{xz}$ [GPa]	2.9 <sup>a</sup>	4.1 <sup>a</sup>	13.7 <sup>b</sup>	6.2 <sup>b</sup>
Poisson's ratio, $x$ - $y$ -plane, $\nu_{xy}$	0.36 <sup>a</sup>	0.31 <sup>a</sup>	0.04 <sup>b</sup>	0.06 <sup>b</sup>
Poisson's ratio $y$ - $z$ -plane, $\nu_{yz}$	0.31 <sup>a</sup>	0.34 <sup>a</sup>	0.24 <sup>b</sup>	0.34 <sup>b</sup>
Poisson's ratio $x$ - $z$ -plane, $\nu_{xz}$	0.31 <sup>a</sup>	0.34 <sup>a</sup>	0.71 <sup>b</sup>	0.42 <sup>b</sup>

<sup>a</sup>Based on available ply data and laminate theory

<sup>b</sup>Predicted by manufacturer, using textile software

<sup>c</sup>Measured [43]

The properties of the NCF laminates are based on laminate theory and experimental data from unidirectional NCF specimens. The predicted properties of the 3D weaves were provided by the manufacturer and were based on their own in-house software for textiles. Tensile tests in the  $x$ -direction indicated that the properties of the LTL weave were accurately predicted, while the properties of the AI weave appear to be severely overestimated. The discrepancy between predicted and measured properties of the AI weave laminates are partly or fully explained by microscopy observations which indicated significant matrix cracking after curing. Inability of the software to accurately predict matrix dominated properties may, however, also have contributed to the discrepancy. Note that the laminates from multidirectional NCF material will be somewhat orthotropic in flexure, and that the degree of flexural orthotropy is influenced by the thickness and stacking sequence.

Specimen types 1 and 2 had dimensions 250 × 250 mm, with a free window of 200 × 200 mm, while specimens 3–5 had length 150 mm and width 100 mm. The length direction is assigned the  $x$ -coordinate and the width direction the  $y$ -coordinate. During cross sectioning of the 3D weave reinforced plates the directions of the warp and weft directions in relation to the  $x$ - and  $y$ -directions of the plates during testing were confirmed, as indicated in Fig. 7.

### 3.3 Impact Testing

The laminates were cut into plates and impacted in the high-speed gas gun impact equipment at Luleå University of Technology in Sweden. The current paper is limited to experiments using 34 and 48 mm diameter ice spheres. Similar tests were also performed with 6 mm diameter runway stones and have been briefly described

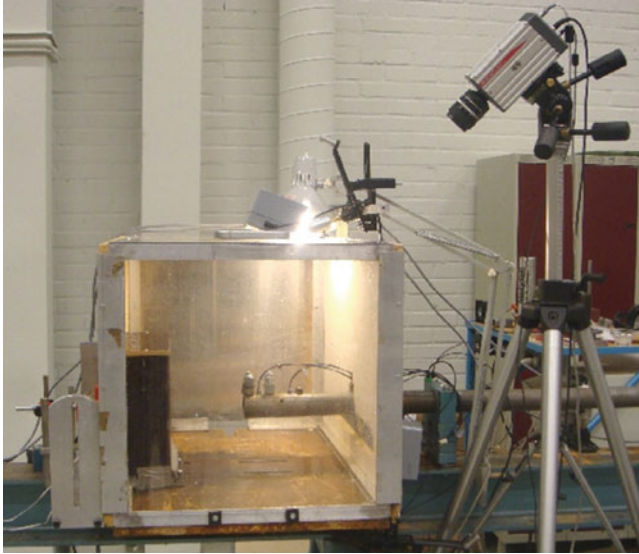


**Fig. 8** Complete test setup [14]

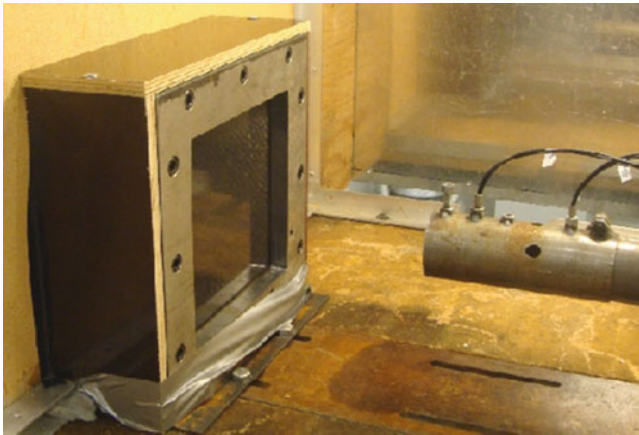


**Fig. 9** Steel rig with plate and pipe end [14]

in [13]. The experiments were followed by a fractographic investigation consisting of visual inspection, ultrasonic C-scan analysis, optical microscopy and Scanning Electron Microscopy (SEM).

The gas gun consisted of a compression tank connected to a steel pipe approximately 5 m long with an inner diameter of 52 mm. The end of the pipe was placed inside a box where the plates were fastened approximately 200 mm from the pipe end using a steel rig, see Figs. 8 and 9.

**Fig. 10** Centre cross-section of the steel rig, view from above [14]

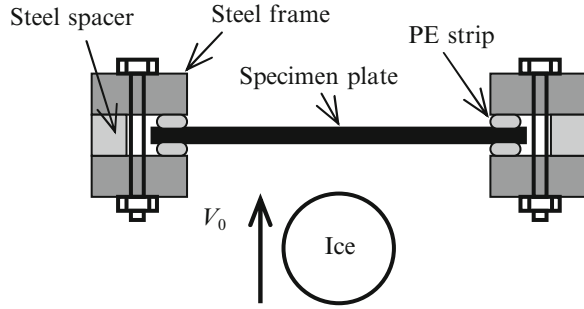


**Fig. 11** Moulded ice ball [14]



The steel rig was made of three parts, front and back plates, width and height 300 and 20 mm thick with a steel spacer in between. The plates were mounted in the rig using steel bolts with a plexi-glass strip in front and a polyethylene (PE) strip in the back of the plates, see Fig. 10. The polymer strips were 5 mm thick and the clamping was made to compress the PE strip approximately 1 mm. The open window measured  $200 \times 200$  mm with a radius of 10 mm in the corners.

Ice balls with different diameters,  $\phi = 25$  to 48 mm, were manufactured by filling fresh tap water in squash balls and plastic balls, and allowing air to escape during a period of about 1 week. Subsequently the water was frozen slowly at a temperature of about  $-2^\circ\text{C}$ . Thereafter the temperature was lowered to  $-10^\circ\text{C}$ , which was maintained until testing. The moulded ice balls deviated somewhat from perfect spheres but were of rather high quality in terms of absence of cracks, see Fig. 11, although there were indications of a limited amount of micro-cracks close to the plastic mould filling hole. The mass and average diameter of each ice ball were measured prior to launch using a scale and a caliper, giving an average density of  $\rho_{ice} = 970 \text{ kg/m}^3$ .

A low density cylindrical foam plug (sabot) was used to push the ice balls down the pipe using compressed air. The foam plugs were used to soften the acceleration

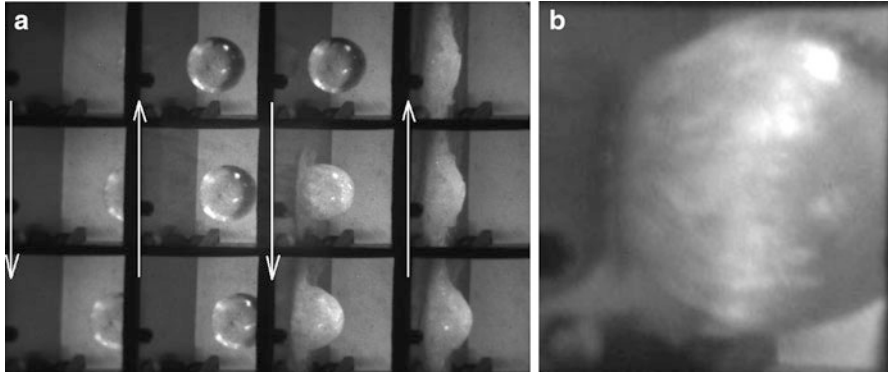


**Fig. 12** Pictures captured by high speed camera. (a) Impact event [13] © Elsevier. Reprinted with permission, (b) Pressure wave in the ice [14]

and protect the ice. The impact speed was measured using two laser sensors placed at a specific distance between each other close to the pipe end, see Fig. 9.

Centre displacements of the plate and ice impact velocity were recorded for all materials tested (see Sect. 3.2). For the NCF laminates strain gauges (Kyowa KFRP-2-120-C1-3L1M3R, 2 mm gauge length, 120  $\Omega$ ) were also applied on the back of the plates, one in the centre and one 50 mm off centre. Both were applied in the direction of the surface ply direction to increase the ability for measurement after initiation of matrix cracks. The strains were registered using a half bridge amplifier with a bandwidth of 100 kHz. The deflections and strains were registered using a sampling frequency of 1 MHz. The impact events were recorded using high speed video (MotionPro X3 Plus, Red Lake) using a sampling frequency of approximately 6,000 frames per second. After impact an ultrasound equipment (Sonatest 380 M with Sonatest 5 MHz/0.5 in. probe) was used to monitor damage initiation (delamination) in the plates.

### 3.4 Experimental Results

In the experiments, a pressure wave forms at the point of contact and moves towards the back of the ice ball. The wave creates micro cracks which suddenly transforms the ice from a solid body to a body made up of small ice particles. A small rise in the strain response can be seen just prior to when the equator of the ball reaches the plate, which is probably related to the momentum of the ball. Figure 12 illustrates the impact scenario. The pictures in Fig. 12a should be read from the first column on the left going down, second column going up etc. Figure 12b shows a snapshot of the pressure wave (white band) travelling from the impact point.

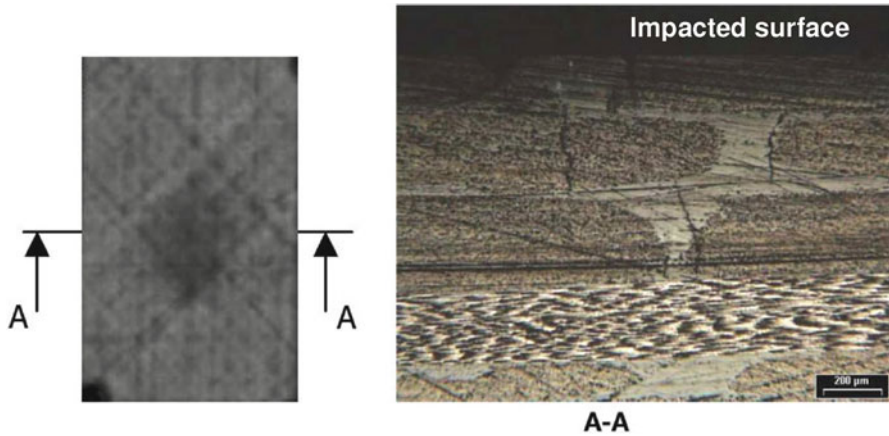
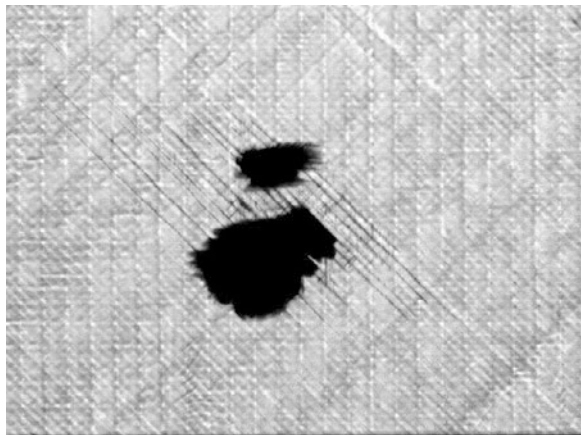


**Fig. 13** Matrix cracks at the impact point. Ultrasound image and polished cross-section of an NCF laminate [13] © Elsevier. Reprinted with permission

**Fig. 14** Ultrasound image of damage after impact



Investigations of the impacted plates show a typical damage initiation and progression response. When the damage threshold velocity is exceeded, damage appears as transverse matrix cracks at the impact point, see Fig. 13. As the impact velocity increases delaminations appear, growing in size as the velocity increases, see Fig. 14.

Interlaminar delaminations typically appear for a laminated composite material. For the 3D-weaves other damage types generally appear as well, such as fibre tensile breakage, fibre kinking and fibre-matrix debonding see Figs. 15 and 16.

Figure 17 gives a comparison of the visually detected damage for the 2D plain weave and the two 3D weaves at different normalised impact velocities. Subsequent

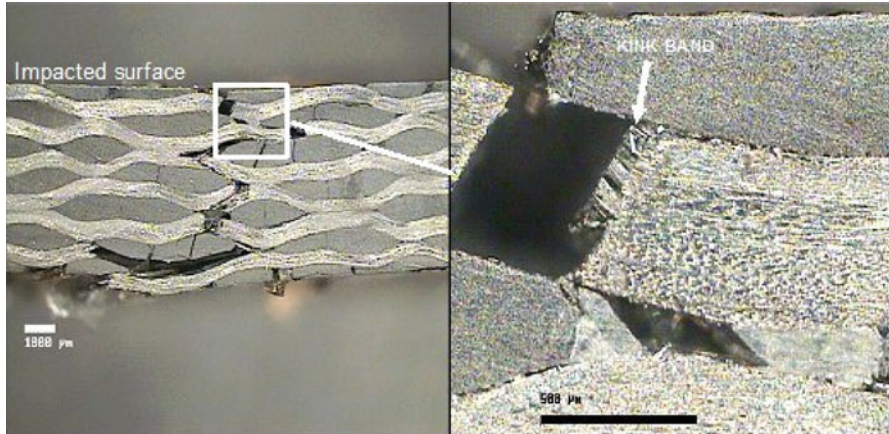


Fig. 15 Damage in 3D angle interlock (AI) weave

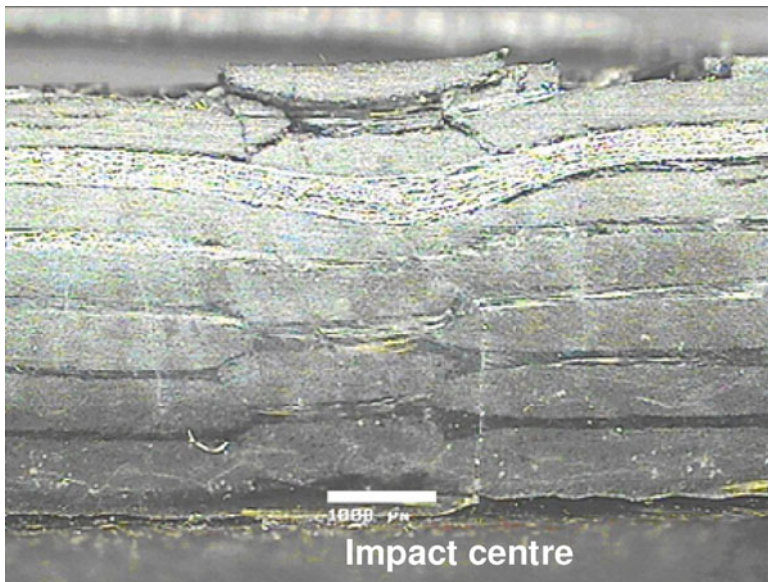
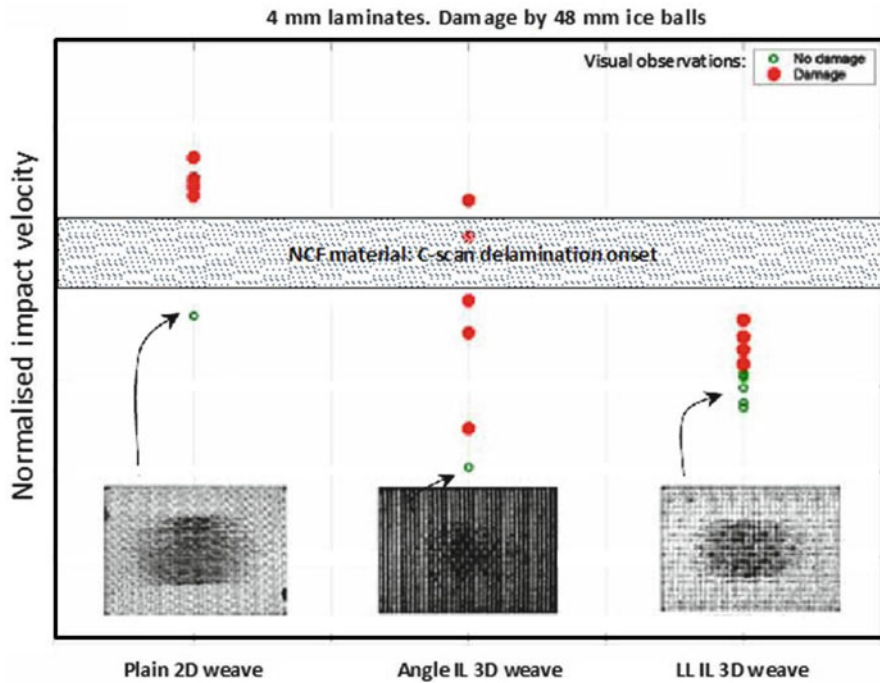


Fig. 16 Damage in 3D layer-to-layer (LTL) interlock weave

C-scans have been included together with arrows indicating the corresponding velocity, and show that large delaminations were present well before visible damage. The velocity range where delamination was detected by C-scan in the reference NCF-system has also been included for comparison. It is noted that delaminations in the woven laminates were present at much lower velocities than in the NCF



**Fig. 17** Comparison of damage in NCF and weaves at different normalised impact velocities

laminates. The more extensive damage may partly be explained by the fact that fractography indicated that the fibre-matrix adhesion was not optimal for the woven laminates, which were based on a different fibre/matrix system than the NCF laminates. Nevertheless, all woven laminates contained a common fibre/matrix system and it is noted that an *increasing* degree of fibres in the thickness direction, i.e. the progression from 2D Plain Weave via Layer-To-Layer interlock 3D weave to Angle Interlock 3D weave, resulted in a *decreasing* damage threshold velocity. The extensive damage in the angle interlock system appears to have been caused by excessive deformation of the fibre bundles during the RTM process and by extensive matrix cracking after curing, which were observed on micrographs prior to testing. The matrix cracks are reflected by the black bands in the C-scan, which are present outside the delamination zone of the angle interlock 3D weave in Fig. 17.

The centre strain gauge readings (NCF material), Fig. 18a, show an initial peak corresponding to the first impact, and a second peak due to the arrival of the major flexural wave after reflection at the boundaries. Figure 18b illustrates a typical behaviour for the strain gauge located 50 mm off-centre.

The response illustrated in Fig. 18a indicates that the delamination threshold velocity is controlled by the peak load (peak centre strain) occurring just after the

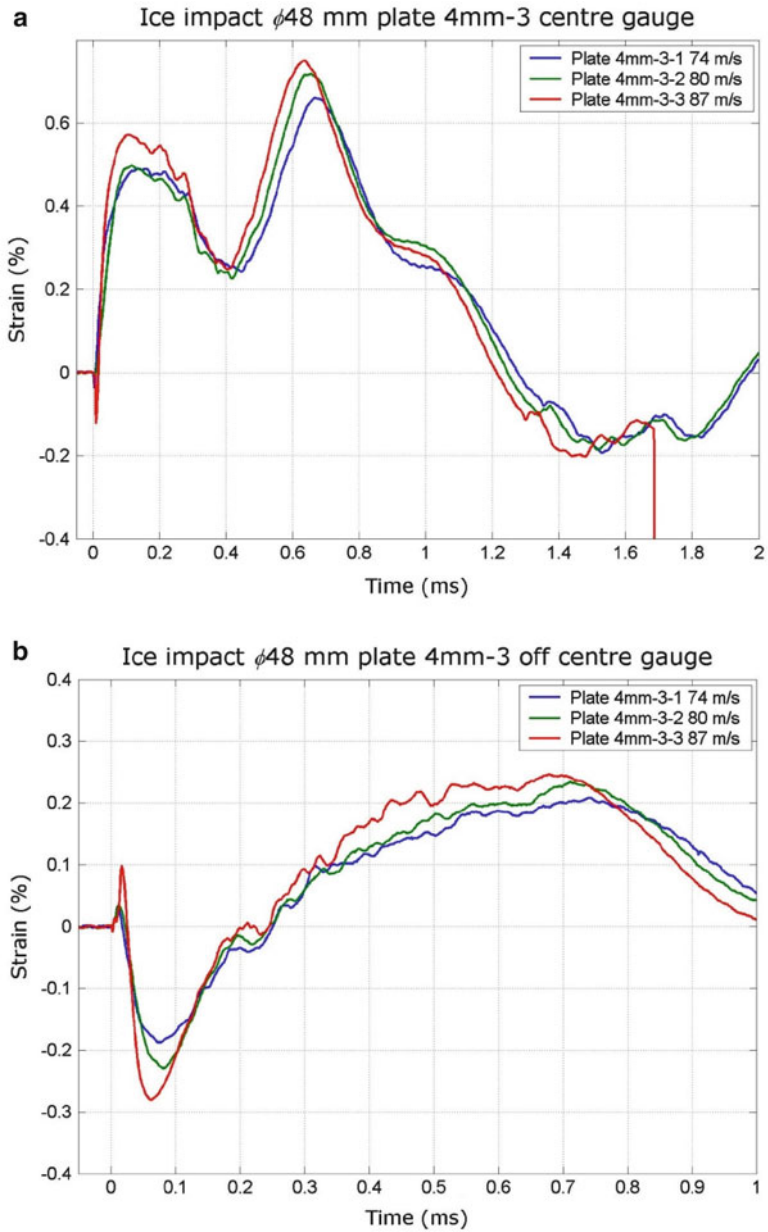


**Fig. 18** Experimental strain history from ice impact. Strain response at (a) the centre and (b) off-centre

initial linear response. The FE simulations and previous analytical work [44], show a very strong link between the contact load and local flexural strains. Hence, the centre strain history also gives an indication of the impact load history.

## 4 Finite Element Simulations

The numerical modelling part was divided into calibrating the ice material model and predicting the threshold velocity for initiation of damage (delamination). All calculations were carried out using LS-Dyna.

The calibration of the ice material model was performed by choosing a representative material model and a parameter fitting procedure. The model is similar to the elastic–plastic ice model used in [32]. Two experiments were chosen to calibrate the model, one using a  $\phi 34$  mm ice ball and one using a  $\phi 48$  mm ice ball. The velocity in both tests was beneath the delamination initiation threshold velocity. A factorial parameter study was performed to identify how the material model parameters influenced the impact response. The factorial study was followed by a fitting of the parameters to the experimental results.

The plate was modelled using layered thick shell elements for the plate and Smooth Particle Hydrodynamics (SPH) for the ice ball. Four layers of thick shell elements (6 plies in each element layer) with full 3D stress updating were used through the thickness of the plate. Figure 19 illustrates the FE model.

For prediction of delamination initiation and growth a layer of solid cohesive elements of thickness  $t_{coh} = 0.01$  mm was included in the centre of the laminate, where the highest shear stresses are expected. The cohesive elements (LS Dyna no. 138) allow for mixed mode tensile-shear interaction using bilinear cohesive laws with linear softening after failure initiation. Hence, each material is modelled by the

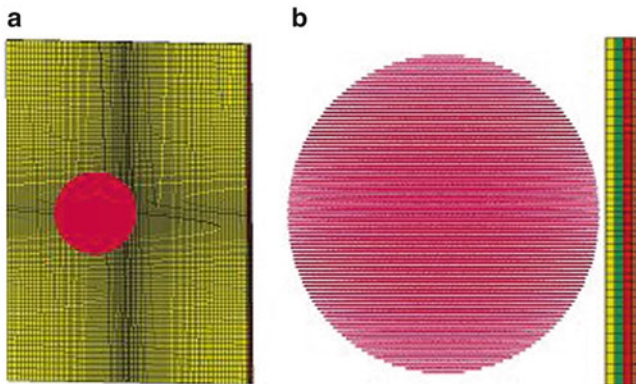


**Fig. 19** FE model of the ice impact: (a) complete model, (b) close up of the ball and the centre of the plate [14]

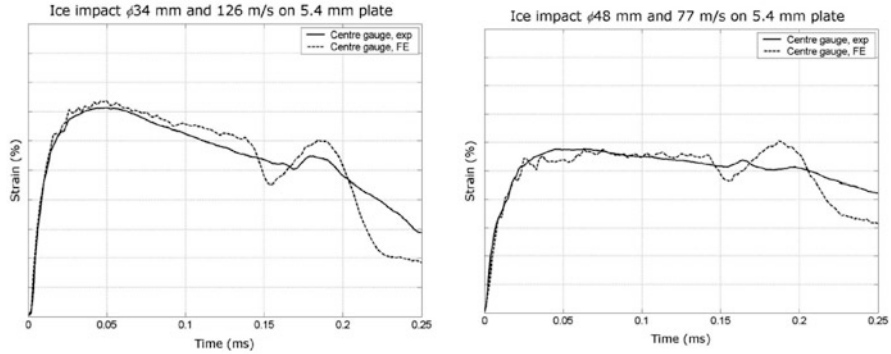


**Fig. 20** Comparison of strain response between experiment and FE simulation after calibration of the ice material model [14]

interlaminar toughness values  $G_{Ic}$  and  $G_{IIc}$  ( $G_{IIIc}$  is assumed equal to  $G_{IIc}$ ), and the interlaminar tensile strength  $T$  and shear strength  $S$ . The corresponding normal ( $EN$ ) and tangential ( $ET$ ) stiffness of the cohesive element were set to  $EN = E_{33}/t_{coh}$  and  $ET = G_{13}/t_{coh}$ . Interlaminar toughness and strength were either based on published data or on available in-house experimental data.

The computational approach is demonstrated here on the quasi-isotropic carbon/vinyl ester NCF laminate (specimen type 1). The material properties used in the analysis were listed in Table 3. Further details on the experiments may be found in [14].

The modelling of the damage initiation threshold velocity was performed for four different ice ball diameters,  $\phi 25$ ,  $\phi 34$ ,  $\phi 40$  and  $\phi 48$  mm. Experimental results were only available for the  $\phi 34$  and  $\phi 48$  mm ice ball impacts, the other two were performed to give a more thorough comparison with the analytical model. The result of the calibration of the ice material model is shown in Fig. 20. The fidelity of the ice model is also supported by the ability to capture the stress wave in the ice and the subsequent microcracking, c.f. Figs. 12 and 21.

The predicted delamination threshold velocities, and corresponding experimental results, for the 5.4 mm carbon fibre/vinyl ester biaxial NCF laminates are given in Fig. 22. Further details and material data on these experiments can be found in [14]. The delamination threshold velocity was found by gradually increasing the impact velocity until delaminations were detected using ultrasonic equipment. In this case only two panels were available for testing and the tests with the 48 mm diameter ice ball were interrupted before the delamination threshold velocity was reached. A good agreement between predictions and experiments has, however, also been found in simulations performed in more extensive confidential studies of quasi-isotropic carbon/epoxy NCF laminates of different thickness.

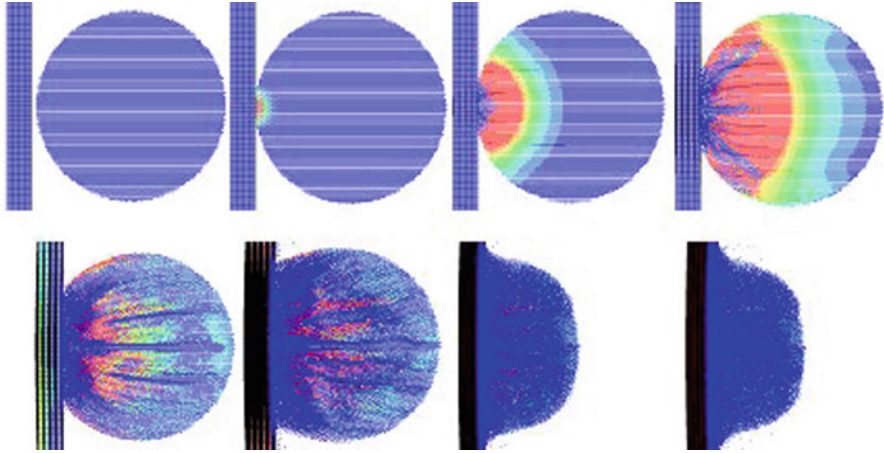


Fig. 21 Pictures from FE simulation of the Ø48 mm ice impact [14]

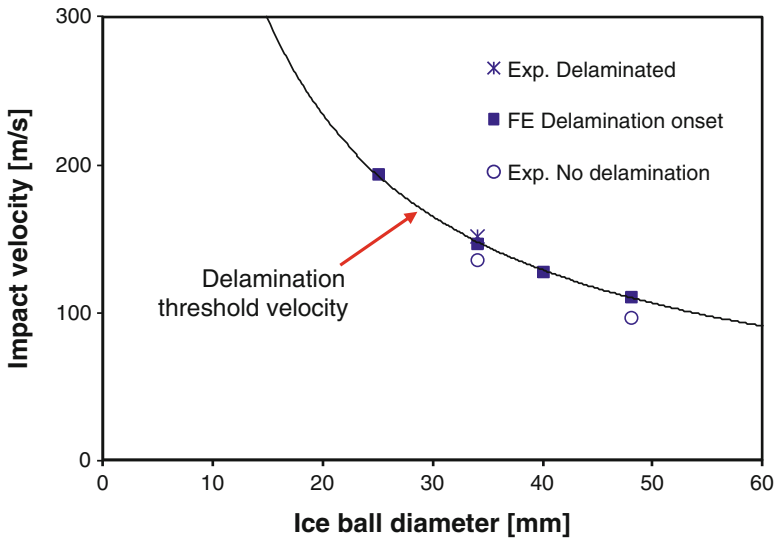
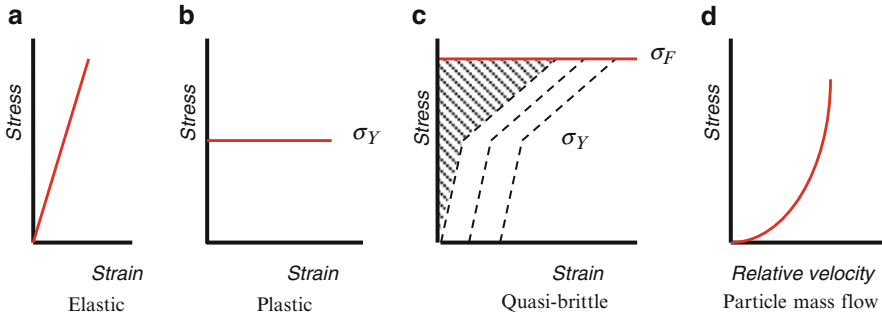


Fig. 22 Comparison between FE predictions of delamination onset and experimental observations for a 5.4 mm carbon/vinyl ester NCF laminate [14]

## 5 Analytical Models

### 5.1 Impact Response Up to Delamination Onset

An analytical response model was developed for fast numerical simulation of hail impact [15]. The model is based on a model for small mass impact on thin



**Fig. 23** Material models considered in the analytical impact model

orthotropic plates [45], which has been modified to account for a finite contact area and various constitutive models for the impactor. The underlying assumptions of the model are as follows:

- The plate region affected by impact through flexural and shear waves is smaller than the total size of the plate
- The contact area is much smaller than the affected region of the plate
- Through-the-thickness waves do not affect the contact behaviour (i.e. quasi-static contact applies).

Four different material models were considered for the ice ball; (a) fully elastic, (b) ideally plastic, (c) quasi-brittle, (d) mass flow of particles, Fig. 23. Failure of the quasi-brittle material was assumed to occur as a sequence of brittle failures at the ultimate failure stress  $\sigma_F$ . Figure 23c illustrates a sequence of elastic–plastic loading curves (dashed) with brittle failure at  $\sigma_F$ , and the corresponding simplified material model (solid line), together with the neglected initial behaviour (shadowed area). For the particle cloud no cohesive forces are present and the contact pressure is equal to the dynamic pressure from the mass flow against the plate, Fig. 23d.

For comparison with FE simulations a 48 mm diameter ice ball impacting the centre of a plate with dimensions  $200 \times 200 \times 6.15$  mm was considered. The plate considered consists of carbon/epoxy NCF material with the layup  $(45/0/-45/90)_{3s}$ . A mode II interlaminar toughness  $G_{IIc} = 1,420$  J/m<sup>2</sup> was assumed, [46]. The quasi-brittle ice model was based on the data in [32]. The material properties assumed for the composite plies and the quasi-brittle ice are listed in Table 2. For the composite plies index 1 refers to the fibre bundle direction, 2 and 3 to the in-plane and out-of-plane directions transverse to fibre bundles. For the ideally plastic ice  $E_{pl}$  was set to 0.001 GPa and  $\varepsilon_{plF}$  to 1,000.

The approach  $\alpha$  (“indentation”) between the impactor and plate may be expressed through the displacements  $w_i$  of the ice impactor and  $w_p$  of the plate centre, which are given as follows [45]:

$$\begin{aligned}
 \alpha = w_i - w_p = & \underbrace{V_0 t}_{\text{Free impactor movement}} - \underbrace{\frac{1}{M} \int_0^t F(\tau) (t - \tau) d\tau}_{\text{Impactor retardation}} - \underbrace{\int_0^t \frac{F(t)}{8\sqrt{mD^*}} \frac{2}{\pi} \arctan \left[ \frac{(t - \tau) S^*}{\sqrt{mD^*}} \right] d\tau}_{\text{Plate bending deflection}} \\
 & + \underbrace{\int_0^{t-t_0} \frac{F(t) d\tau}{2\pi S^* (t - \tau)}}_{\text{Plate shear deflection}}
 \end{aligned} \tag{1}$$

where  $V_0$  is the impact velocity,  $M$  is the impactor mass,  $F$  is the resulting contact load,  $m$  is the mass per unit area of the plate,  $D^*$  is an effective bending stiffness of the plate,  $S^*$  is a corresponding shear stiffness,  $t$  is time,  $t_0$  is a time correction accounting for finite contact area and  $\tau$  is dummy integration variable. The time constant  $t_0$  and the effective bending and shear stiffness  $D^*$  and  $S^*$  of orthotropic laminates are given by the following expressions:

$$\begin{aligned}
 D^* &\approx \sqrt{D_{11} D_{22} (1 + \eta) / 2} \quad \text{where} \quad \eta = (D_{12} + 2D_{66}) / \sqrt{D_{11} D_{22}} \\
 S^* &\approx \sqrt{A_{44} A_{55}} = \sqrt{K_{yz} G_{yz} h K_{xz} G_{xz} h} \quad t_0 = R\alpha \sqrt{m / D^*} / 4
 \end{aligned} \tag{2}$$

where  $D_{ij}$  and  $A_{44}, A_{55}$  are the bending and transverse shear stiffnesses according to laminated plate theory,  $K_{ij}$  are shear factors ( $\approx 5/6$ ),  $h$  is the plate thickness, and  $R$  is the radius of the impactor (ice ball).

The contact load may be obtained from the following relation [15]:

$$F = p_{av} \pi c^2 \quad \text{where} \quad \begin{cases} c^2 = R\alpha & \text{for elastic contact} \\ c^2 = 2R\alpha - \alpha^2 & \text{for plastic contact} \end{cases} \tag{3}$$

where  $c$  is the contact radius. The contact radius for plastic conditions is obtained from a purely geometrical relation, assuming no material pile up at the contact edge.

The average contact pressure  $p_{av}$  is given by the following expressions [15]:

<p>Elastic material</p> $p_{av} = \frac{4}{3\pi} Q_\alpha \sqrt{\alpha / R}$ <p>Quasi – brittle</p> $p_{av} = \sigma_F$	<p>Plastic material</p> $p_{av} = 2.8\sigma_Y$ <p>Particles</p> $p_{av} = \frac{1}{2} \rho_i (V_0 - \dot{w}_p)^2$
---	---

where  $Q_\alpha$  is an effective contact modulus,  $\sigma_Y$  is the yield stress,  $\sigma_F$  is the ultimate compressive strength and  $\dot{w}_p$  is the deflection velocity of the plate at the point of impact. All cases, except the elastic, have more or less uniform contact pressure

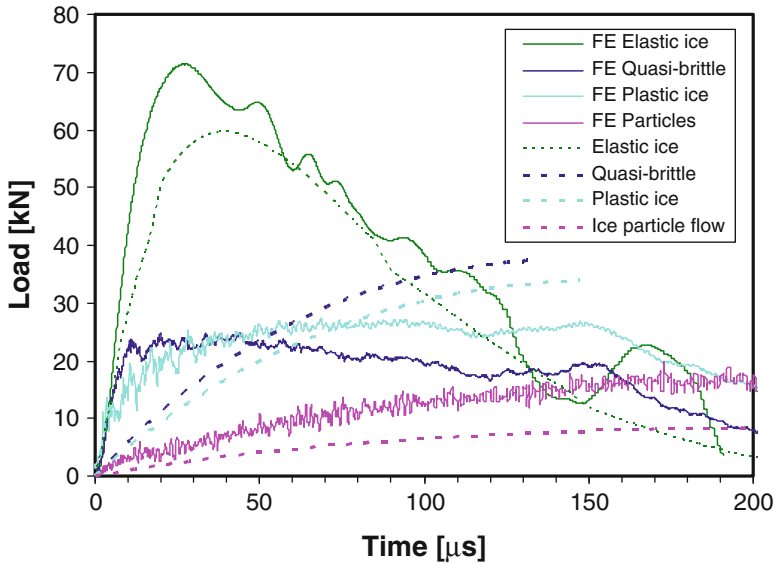


Fig. 24 Effect of various ice models during 117 m/s impact on elastic plate [15]

distributions. The average contact pressure for plastic contact is based on empirical findings by Tabor in 1951 from experiments with rigid hemispheres indenting ideally plastic plates, and a later theoretical study [47] which also demonstrated that the contact stress under ideally plastic contact is relatively *uniform*. By inserting Eq. (3) in Eq. (1) we obtain an integral equation for the indentation  $\alpha$ . This equation may be written on a dimensionless form and solved numerically in a stepwise fashion, as described in [45].

Figure 24 gives a comparison of the analytically predicted load histories and the corresponding FE-simulations for a 48 mm diameter ice ball impacting the 6.15 mm thick plate at 117 m/s. According to the FE simulations this was just below the delamination threshold velocity for a quasi-brittle impactor but all analyses were performed assuming a fully elastic plate, i.e. without allowing damage growth. The FE load history is based on the resultant force of the FE contact elements. Figure 24 illustrates that the impact load predicted by FE initially is much higher than predicted analytically. For the homogeneous ice models this effect gradually dies out but for the particle flow the load enhancement appears to prevail through the entire impact, presumably as this is a continuous sequence of separate impacts.

### 5.2 Model for Delamination Onset

Delamination growth in composite laminates is typically generated by coalescence of shear cracks which appear at fairly low loads and grow under an increasing load

until the delamination threshold load is reached. Contact with a crushing ice ball causes a fairly uniform contact pressure,  $p_{av}$ . In this case the midplane (maximum) shear stress at a radius  $a$  is given by the following expression:

$$\tau_{mid} = \frac{3}{2} \frac{p_{av} \pi a^2}{2\pi ah} \Leftrightarrow \tau_{mid}^2 = \frac{9}{16} \frac{p_{av} a}{h} \frac{F(a/c)^2}{\pi ah} = \frac{9}{16\pi} \frac{p_{av} F \bar{a}^2}{h^2} \quad (5)$$

where  $\bar{a} = a/c$

The critical contact force  $F_{sc}$  for shear cracking at a radius  $a$  at a given shear strength  $\tau_c$  is obtained by the expressions:

$$\begin{aligned} F_{sc} &= \frac{16\pi}{9} (\tau_c h / \bar{a})^2 / p_{av} & \text{for } \bar{a} = a/c \leq 1 \\ F_{sc} &= \frac{16\pi}{9} (\tau_c h)^2 \bar{a} / p_{av} & \text{for } \bar{a} = a/c \geq 1 \end{aligned} \quad (6)$$

Expressions for the critical load for delamination growth were provided in [15] and are as follows:

$$\begin{aligned} \bar{a} = \infty : F_{dth} &= C F_{d1F} \quad \text{where } C = 1.213 \quad \text{and } F_{d1F} = \pi \sqrt{32DG_{IIc}/3} \\ \bar{a} \gg 1 : F_{dth} &\approx C F_{d1F} \cdot \sqrt{w(c=0)/w(c \neq 0)} \\ 1 \leq \bar{a} \approx 1 : F_{dth} &\approx F_{d1F} \sqrt{12/\bar{a}} \\ \bar{a} < 1 : F_{dth} &= F_{d1F} 2 / (1 - \bar{a}^2) \end{aligned} \quad (7)$$

The first expression is based on the closed form solution in [6], while the fourth expression is based on a closed form solution in [48]. The second and third expressions are based on perturbations of the first and fourth expression, as described in [15]. By comparison of Eqs. (5) and (6) it is obvious that shear cracks will initiate at the edge of the contact area ( $\bar{a}=1$ ) and will grow inwards and outwards until the critical load for delamination growth is reached. Subsequent delamination growth inwards and outwards will occur under a decreasing load. The process is illustrated in Fig. 25, where the curve for delamination growth outside the contact radius has been obtained by a simple curve fit to data points where the perturbation solutions are considered valid. For the quasi-brittle ice the quasi-static ultimate stress of  $\sigma_F = 35$  MPa results in an analytically predicted delamination load of about 38 kN, which is significantly higher than the FE prediction of 24 kN.

## 6 Causes for Discrepancies Between FE-Simulations and Simplified Analytical Models

To understand the reasons for the discrepancy between the analytical predictions and the FE-simulations the spatial distribution and time histories of the contact pressure in the FE model were examined in detail. The stresses were also compared

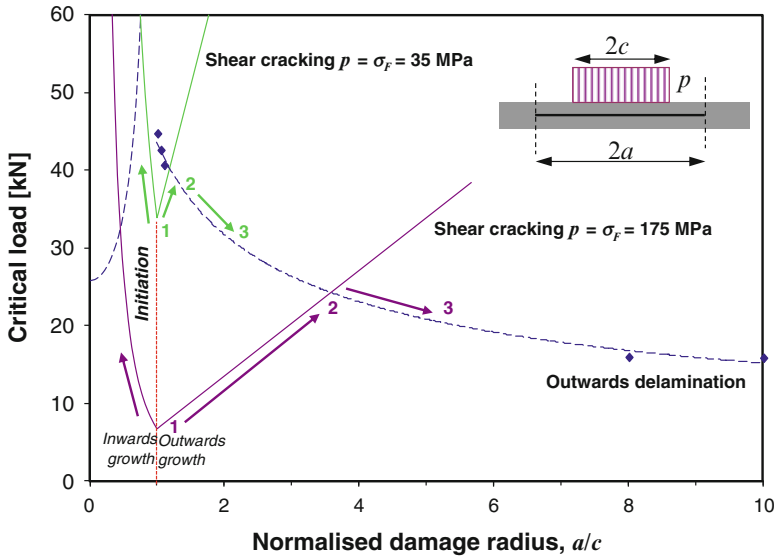


**Fig. 25** Critical loads for shear cracking (*solid lines*) and delamination growth (*dashed lines*) under uniform local pressure by quasi-static crush stress (35 MPa) and initial stress peak (175 MPa)

with the expected average stress, given by the impact load divided by contact area. The contact stresses predicted by the SPH model were essentially “white noise”, although the average stress was in fair agreement with the average stress expected from the load history. For this reason, the stresses at the top surface of the solid shell elements were used for *prediction* of the contact stresses. The LS Dyna thick shell elements with only 2D plane stress update resulted in very low stresses in poor agreement with the expected contact stress, while elements with full 3D stress updating produced stresses in good agreement with the expected contact stress. Figure 26 shows the pressure distribution predicted by the latter elements at some different times, and illustrates that there is a significant variation in the pressure distribution. Further analysis is ongoing to clarify if these fluctuations are due to numerical problems or due to actual wave phenomena. It is noted that the contact stresses after 40  $\mu$ s are in good agreement with the  $\sigma_F = 34.4$  MPa predicted by the material model, while the stresses initially are much higher.

Figure 27 illustrates the contact pressure histories at three different distances ( $x$ ) from the impact centre during impact with a quasi-brittle material. It is noted that the high initial contact pressures gradually approach the quasi-static value of  $\sigma_F$  assumed in the analytical model. The initial stress peak may be explained by propagation of through-the-thickness waves. The stress amplitude can be approximated by the following expression for one-dimensional elastic wave propagation after an impact between two cylindrical elastic bodies [15]:

$$p_{in} = p(t = 0) = \sqrt{\rho_p E_{pz}} V_0 / (1 + \rho_p / \rho_i) \tag{8}$$

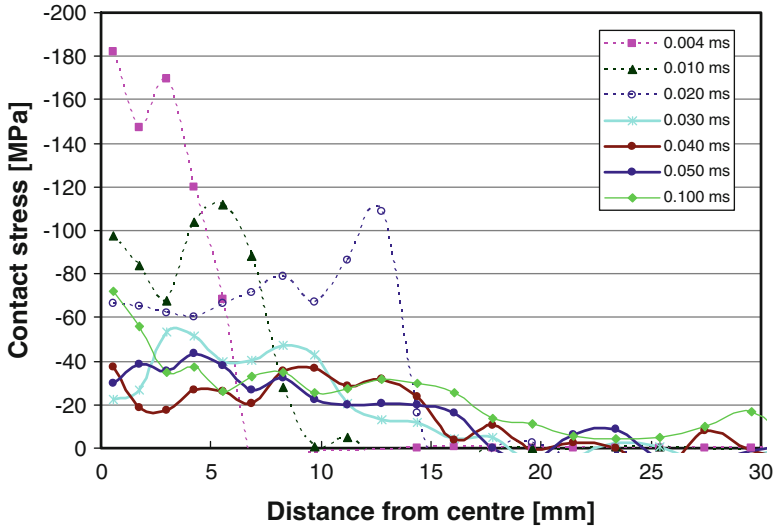


Fig. 26 Contact stress distributions at  $V_0 = 117$  m/s for quasi-brittle material [15]

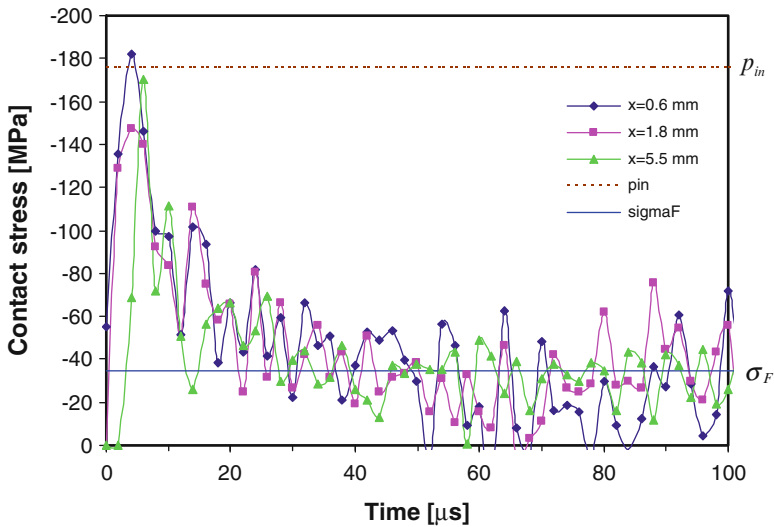
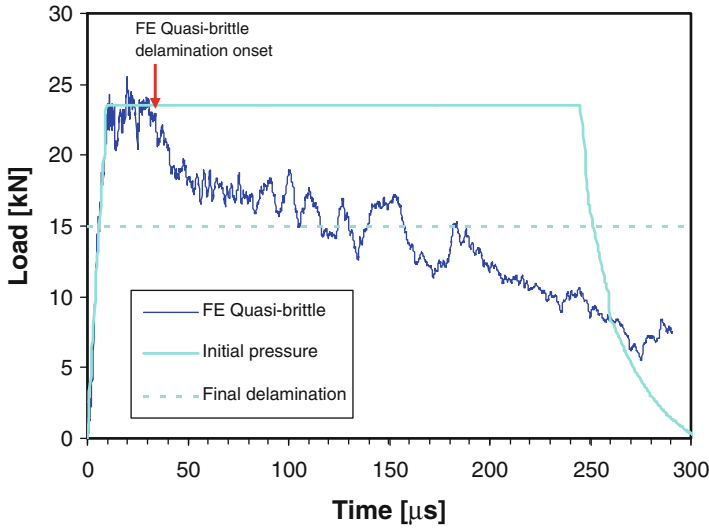


Fig. 27 Decay of contact stresses with time during 117 m/s impact with quasi-brittle impactor ( $x$  is distance from impact centre) [15]

where  $\rho_p$  and  $\rho_i$  are the densities of the plate and impactor and  $E_{pz}$  is the out-of-plane Young's modulus of the plate. The predicted initial peak pressure  $p_{in}$  has been included in Fig. 27, which demonstrates that Eq. (8) gives a fairly accurate prediction of the initial pressure peak.



**Fig. 28** FE-simulation and upper and lower analytical bounds for the load history with quasi-brittle ice impacting at 118 m/s (delamination onset)

The comparatively low contact pressure during ice impact results in higher delamination threshold loads than for equally sized metal impactors. For a uniform pressure equal to the initial stress peak ( $p_{in}$ ) the delamination threshold load indicated by Fig. 25 is about 24 kN, which is followed by delamination growth at a decreasing load.

Figure 28 illustrates analytical simulation of delamination using a modified material model, assuming a uniform contact pressure equal to the initial stress peak ( $p_{in}$ ) until unloading occurs, and a load limited by a delamination threshold value of 24 kN. The initial response is in good agreement with the FE-simulation, which appears to gradually approach the load for quasi-static delamination growth, but the analytical model is unable to model the gradual decay in the load associated with the decreasing contact pressure (c.f. Fig. 27) and delamination growth (c.f. Fig. 28). It may be concluded that an accurate analytical model for hail impact would require incorporation of the initial contact pressure peak and the subsequent decay in contact pressure, as well as delamination initiation criteria considering the effect of a finite contact area.

## 7 Discussion and Conclusions

It may be concluded that the predicted response to hail impact on composite laminates is strongly influenced by the corresponding material model and by three-dimensional wave propagation during the initial phase of the impact. More reliable predictions of damage initiation and growth require development in several areas.

Reliable physically based models must be developed to account for the influence of anisotropy, strain rate, temperature and triaxial stress state for the stiffness and strength of ice under loading conditions relevant to hail impact during flight. This requires both a more thorough review of existing literature on ice behaviour and complementary experiments.

Detailed three-dimensional FE analysis is required for the initial phase of the impact to study the effect of out-of-plane waves and of the heterogeneous structure of laminates. Accurate prediction of the resulting damage also requires models for intralaminar and interlaminar damage growth in each ply and interface of the laminate.

Improved analytical models should be developed by incorporation of the influence of through-the-thickness waves on the initial contact pressure peak and its subsequent decay, as well as appropriate failure criteria to account for a finite contact area. The aim of these models should be to incorporate key mechanisms, while keeping the models sufficiently simple to be useful for preliminary design.

The methods should first be applied to hail of different size impacting plates with a range of different material systems, layups and thickness and validated by accompanying experiments. Subsequently the methods need to be extended to more complex geometries, e.g. leading edges and engine components. Finally the approach should be demonstrated by analysis and testing of a number of realistic components.

**Acknowledgements** Significant parts of the experimental work presented in this paper were funded by the VITAL project (FP6 Contract VITAL AIP4-CT-2004-012271). Further experimental studies have been funded through direct contracts from Volvo Aero Corporation (VAC), and we are grateful for the cooperation with Dr Fredrik Edgren, Dr Niklas Jansson and Mr Anders Sjunnesson at VAC. Further numerical and analytical studies have been funded by the internal competence development funds of the Swerea Group. Parts of the update on recent literature on hail impact have been provided by Dr Renaud Gutkin.

## References

1. Souter RK, Emerson JB (1952) Summary of available hail literature and the effect of hail on aircraft in flight. NACA TN 2734. NACA, Washington, DC
2. Anghileri M, Castelletti L-ML, Invernizzi F, Mascheroni M (2005) A survey of numerical models for hail impact analysis using explicit finite element codes. *Int J Impact Eng* 31: 929–944
3. Field PR et al (2009) Hail threat standardisation. Research project EASA.2008/5, EASA
4. Davies GAO, Olsson R (2004) Impact on composite structures. *Aeronaut J* 108(1089):541–563
5. Mahinfalah M, Skordahl RA (1998) The effects of hail damage on the fatigue strength of a graphite/epoxy composite laminate. *Compos Struct* 42:101–106
6. Olsson R, Donadon MV, Falzon BG (2006) Delamination threshold load for dynamic impact on plates. *Int J Solids Struct* 43(10):3124–3141
7. Olsson R (2003) Closed form prediction of peak load and delamination onset under small mass impact. *Compos Struct* 59(3):340–348

8. Kim H, Welch DA, Kedward KT (2003) Experimental investigation of high velocity ice impacts on woven carbon/epoxy composite panels. *Compos Part A* 34:25–41
9. Rhymer J, Kim H, Roach D (2012) The damage resistance of quasi-isotropic carbon/epoxy composite tape laminates impacted by high velocity ice. *Compos Part A* 43(7):1134–1144
10. Park H, Kim H (2010) Damage resistance of single lap adhesive composite joints by transverse ice impact. *Int J Impact Eng* 37:177–184
11. Appleby-Thomas GJ, Hazell PJ, Dahini G (2011) On the response of two commercially-important CFRP structures to multiple ice impacts. *Compos Struct* 93(10):2619–2627
12. Östman P, Levin K (1994) On the character of neighbouring low energy impact damages in carbon fibre composites. *Advanced structural fiber composites-proceedings. Topical sympos. III 8th CIMTEC-World Ceramics Cong. & Forum on New Material. Techna, Faenza*, pp 615–622
13. Asp LE, Juntikka R (2009) High velocity impact on NCF reinforced composites. *Compos Sci Technol* 69:1478–1482
14. Juntikka R, Olsson R (2009) Experimental and modelling study of hail impact on composite plates. Paper F7:4. In: *Proceedings of the 17th international conference on composite materials, Edinburgh*
15. Olsson R, Juntikka R (2010) Validation of analytical model for hail impact on composite laminates. Paper 137. In: *Proceedings 14th European conference on composite materials, Budapest*
16. AMS Glossary (2012) <http://amsglossary.allenpress.com/glossary>. Accessed 29 Mar 2012
17. Wikipedia (2012) Hail. <http://en.wikipedia.org/wiki/Hail>. Accessed 29 Mar 2012
18. NOAA (2012) National weather service, St. Louis, MO Weather Forecast Office. [http://www.crh.noaa.gov/lx/?n=10\\_18\\_2004](http://www.crh.noaa.gov/lx/?n=10_18_2004). Accessed 22 May 2012
19. NOAA (2012) NOAA Photo Library, NOAA Central Library; OAR/ERL/National Severe Storms Laboratory (NSSL). <http://www.photolib.noaa.gov/htmls/nssl0001.htm>. Accessed 22 May 2012
20. Ralston TD (1980) Yield and plastic deformation of ice crushing failure. In: Pritchard RS (ed) *Sea ice processes and model*. IAHS-AISH, pp 234–245
21. Schulson EM (1999) The structure and mechanical behavior of ice, featured overview. *JOM* 51:21–27. [www.tms.org/pubs/journals/JOM/9902/Schulson-9902.html](http://www.tms.org/pubs/journals/JOM/9902/Schulson-9902.html). Accessed 29 Mar 2012
22. Cole DM (2001) The microstructure of ice and its influence on mechanical properties. *Eng Fract Mech* 68(17–18):1797–1822
23. Petrovic JJ (2003) Review mechanical properties of ice and snow. *J Mater Sci* 38:1–6
24. Kim H, Keune JN (2007) Compressive strength of ice at impact strain rates. *J Mater Sci* 42:2802–2806
25. Shazly M, Prakash V, Lerch BA (2009) High strain-rate behavior of ice under uniaxial compression. *Int J Solids Struct* 46:1499–1515
26. Schulson EM (2001) Brittle failure of ice. *Eng Fract Mech* 68(17–18):1839–1887
27. Masterson DM, Frederking RMW (1993) Local contact pressures in ship/ice and structure/ice interactions. *Cold Reg Sci Technol* 21:169–185
28. Jones SJ (1997) High strain-rate compression tests on ice. *J Phys Chem B* 101(32):6099–6101
29. Arakawa M, Maeno N (1997) Mechanical strength of polycrystalline ice under uniaxial compression. *Cold Reg Sci Technol* 26:215–229
30. Druetz J, Nguyen DD, Lavoie Y (1986) Mechanical properties of atmospheric ice. *Cold Reg Sci Technol* 13:67–74
31. Cox GFN, Richter JA, Weeks WF, Mellor M (1983) A summary of the strength and modulus of ice samples from multi-year pressure ridges. In: *Third international symposium on offshore mechanics and arctic engineering*. New Orleans
32. Kim H, Kedward KT (2000) Modeling hail ice impact damage initiation in composite structures. *AIAA J* 38:1278–1288

33. Schroede RC, McMaster WH (1973) Shock-compression freezing and melting of water and ice. *J Appl Phys* 44:2591–2594
34. Weiss J, Schulson EM (1995) The failure of fresh-water granular ice under multiaxial compressive loading. *Acta Metall Mater* 43:2303–2315
35. Combescure A, Chuzel-Marmot Y, Fabis J (2011) Experimental study of high-velocity impact and fracture of ice. *Int J Solids Struct* 48(20):2779–2790
36. Guégan P, Othman R, Lebreton D, Pasco F, Villedieu P, Meyssonnier J, Wintenberger S (2011) Experimental investigation of the kinematics of post-impact ice fragments. *Int J Impact Eng* 38(10):786–795
37. Carney KS, Benson BJ, DuBois P, Lee R (2006) A phenomenological high strain rate model with failure for ice. *Int J Solids Struct* 43(25–26):7820–7839
38. Chuzel Y, Combescure A, Nucci M, Ortiz R, Perrin Y (2010) Development of hail material model for high speed impacts on aircraft engine. In: 11th international LS-Dyna users conference
39. Sain T, Narasimhan R (2011) Constitutive modeling of ice in the high strain rate regime. *Int J Solids Struct* 48:817–827
40. VITAL (2009) [http://cordis.europa.eu/projects/rcn/94198\\_en.html](http://cordis.europa.eu/projects/rcn/94198_en.html). Accessed 22 May 2012
41. Edgren F, Soutis C, Asp LE (2008) Damage tolerance analysis of NCF composite sandwich panels. *Compos Sci Technol* 68(13):2635–2645
42. Compston P, Jar P-YB (1998) Comparison of interlaminar fracture toughness in unidirectional and woven roving marine composites. *Appl Compos Mater* 5:189–206
43. Holmberg A, Lundmark P (2006) Composites based on 2-D and 3-D textile preforms. CR 06–013 (Confidential report). Swerea SICOMP, Piteå, Sweden
44. Olsson R (1992) Impact response of orthotropic composite laminates predicted from a one-parameter differential equation. *AIAA J* 30:1587–1596
45. Olsson R (2010) Analytical model for delamination growth during small mass impact on plates. *Int J Solids Struct* 47(21):2884–2892
46. Jain LK, Dransfield KA, Mai Y-W (1998) On the effects of stitching in CFRPs—II. Mode II delamination toughness. *Compos Sci Technol* 58:829–837
47. Biwa S, Storåkers B (1995) An analysis of fully plastic Brinell indentation. *J Mech Phys Solids* 43:1303–1333
48. Davies GAO, Robson P, Robson J, Eady D (1997) Shear driven delamination propagation in two dimensions. *Compos Part A* 28:757–765